

Concurrent Segmentation and Localization for Tracking of Surgical Instruments

Iro Laina^{1*}, Nicola Rieke^{1*}, Christian Rupprecht^{1,2}, Josué Page Vizcaíno¹,
Abouzar Eslami³, Federico Tombari¹, and Nassir Navab^{1,2}

¹ Computer Aided Medical Procedures, Technische Universität München, Germany

² Johns Hopkins University, Baltimore, USA

³ Carl Zeiss MEDITEC München, Germany

Nicola.Rieke@tum.de

Abstract. Instrument tracking is an essential requirement for various computer-assisted interventions. To overcome problems such as specular reflection and motion blur, we propose a novel method that takes advantage of the interdependency between localization and segmentation of the tool. In particular, we reformulate the 2D pose estimation as a heatmap regression and thereby enable a robust, concurrent regression of both tasks. Throughout experimental results, we demonstrate that this modeling leads to a significantly higher accuracy than directly regressing the tool's coordinates. The performance is compared to state-of-the-art on a Retinal Microsurgery benchmark and the EndoVis Challenge.

1 Introduction and Related Work

In recent years there has been significant progress towards computer-based surgical assistance in Minimally Invasive Surgery (MIS) and Retinal Microsurgery (RM). One of the key components for achieving this goal is tracking and segmentation of surgical instruments during the intervention. Possible applications include proximity estimation to the retina in RM via tracking, or detecting suitable regions for a graphical overlay of additional information without obstructing the surgeon's view. Marker-free approaches are particularly desirable for this task as they do not interfere with the surgical workflow or require modifications to the tracked instrument. Despite recent advances, the vision-based tracking of surgical tools in *in-vivo* scenarios remains challenging, as summarized by Bouget *et al.* [1], mainly due to nuisances such as strong illumination changes and blur. Prior work in the field relies on handcrafted features, such as Haar wavelets [2], HoG [3,4] or color features [5], which come with their own advantages and disadvantages. While color features, for example, are computationally cheap, they are not robust towards strong illumination changes which are often present during the surgery. Gradients, on the other hand, are not reliable to withstand the typical motion blur of the tools. Rieke *et al.* [6] employed both feature types in two

* I. Laina and N. Rieke contributed equally to this work.

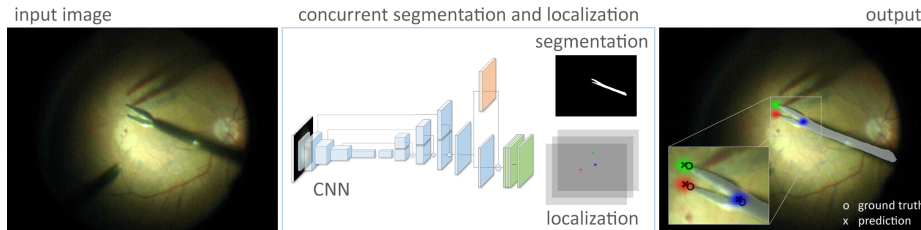


Fig. 1. CSL The segmentation and landmark localization is estimated concurrently.

separate Random Forests and proposed to adaptively choose the more reliable one, depending on the confidence of the respective forest’s leaf nodes. Since their explicit feature representation incorporates implicit simplifications, this tends to limit the generalization power of the forests, and therefore leads to risk of tracking failure during surgery. Sarikaya *et al.* [7] presented a deep learning approach for tool detection via region proposals. However, their algorithm provides only a bounding box and not a precise localization of the landmarks. Instead of tracking the tool directly, two-step methods based on instrument segmentation have also been proposed. Color, HOG and SIFT features were employed by Allan *et al.* [8] for pixel-wise classification of the image. The tool position was subsequently determined based on largest connected components. Instead of reducing the region of interest, Reiter *et al.* [9] employ the segmentation as a post-processing step for improving the localization accuracy by removing outliers. This suggests that the tracking of an instrument landmark and its segmentation are not only dependent, but indeed interdependent.

Our contributions are as follows. Instead of carrying out tool segmentation and pose estimation as two subsequent pipeline stages, we propose to learn and perform the two tasks simultaneously, in a unified approach. To this end, we reformulate the pose estimation task and model the problem as regressing a heatmap where every element represents a confidence proportional to its proximity to the correct landmark location. This modelling allows for representing semantic segmentation and localization with equal dimensionality, which leverages on their interdependency and facilitates simultaneous learning. It also enables employing state-of-the-art deep learning techniques, such as Fully Convolutional Residual Networks [10,11]. The resulting model is trained jointly and end-to-end for both tasks, relying only on contextual information, thus being capable of reaching both objectives efficiently without requiring any post-processing technique. We compare the performance of the proposed method to state-of-the-art algorithms on a benchmark dataset of *in-vivo* RM sequences and on the EndoVis Challenge⁴. To the best of our knowledge, this is the first approach that employs deep learning for surgical instrument tracking by predicting segmentation and localization simultaneously and is successful despite limited data.

⁴ MICCAI 2015 Endoscopic Vision Challenge Instrument Segmentation and Tracking Sub-challenge <http://endovissub-instrument.grand-challenge.org>

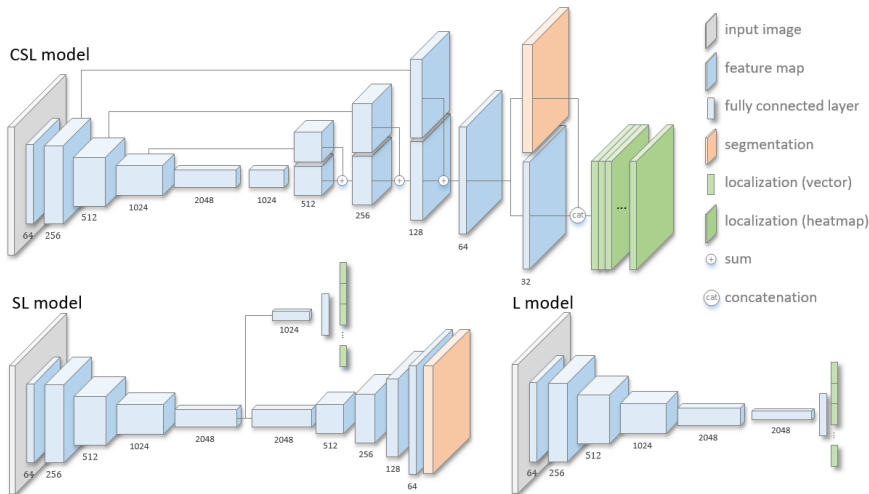


Fig. 2. Modeling Strategies The proposed CSL architecture and two baselines.

2 Method

This section describes our CNN-based approach to model the mapping from an input image to the location of the tool landmarks and the corresponding dense semantic labeling. We motivate the use of a fully convolutional architecture, that models the problem of landmark localization as that of regressing a set of heatmaps, one for each landmark, in combination with semantic segmentation. This approach, which exploits global context to identify the position of the tool, has clear advantages comparing to patch-based techniques [12], which rely only on local information, thus being less robust in false positives arising from, e.g., reflections of the instrument. We compare the proposed architecture and discuss its advantage over two baselines. A common block for all architectures is the encoder (Sec. 2.1), which progressively down-samples the input image through a series of convolutions and pooling operations. The models then differ in the following *decoding* stages (Sec. 2.2) and the formulation of their outputs. An overview is depicted in Fig. 2. We denote a training sample as (X, S, y) , where $y \in \mathbb{R}^{(n \times 2)}$ refers to the 2D coordinates of the n tracked landmarks in the image $X \in \mathbb{R}^{w \times h \times 3}$ and $S \in \mathbb{R}^{\frac{w}{2} \times \frac{h}{2} \times c}$ represents the semantic segmentation of c labels. w and h denote image width and height respectively.

2.1 Encoder

As for the encoding part of the three proposed network models, we employ ResNet-50 [11], a state-of-the-art architecture that has exhibited top performance in several tasks in the field of computer vision, such as classification, segmentation and object detection. It is composed of multiple basic blocks that are serially connected to each other and introduces shortcut connections summed

after every few layers, so as to represent residual functions. In such way, it allows for a very deep architecture without hindering the learning process and at the same time shows less complexity in comparison to other networks of even smaller depth. Although deeper versions of ResNet exist, we use the 50-layer variant, as computation time is still crucial for this task. We enhance the encoder stages by doubling the typical input size to $w = h = 480$. Thus, the last convolutional layer results in 2048 feature maps of spatial resolution 15×15 pixels. The last pooling layer and the loss layer from ResNet-50 are removed.

2.2 Decoder Tasks

Appended to the same encoder block, we define three different CNN variants that aim at three different tasks. In the following we outline the characteristics of such tasks and motivate the choice of the final proposed model.

Localization (L): First, we examine the naïve approach frequently used in literature [13] that regresses the 2D locations of the landmarks directly, while the segmentation task is excluded. For this purpose, we add another residual block [11] with stride to the end of the encoder, in order to further reduce the dimensionality of the feature maps to $8 \times 8 \times 2048$, followed by a 8×8 average pooling layer and a fully-connected layer that produces the output. The dimensionality reduction using strided convolutions is needed such that the averaging is not applied over a large region, which would result in spatial information being lost, hindering the precision with which the network is able to localize. The network is trained by using a standard L_2 loss: $l_L(\tilde{y}, y) = \|\tilde{y} - y\|_2^2$. The training sample in this case is (X, y) and the predicted location is $\tilde{y} \in \mathbb{R}^{2 \times n}$.

Segmentation and Localization (SL): In this model (see Fig. 2 model SL), we regress the 2D locations and predict the semantic segmentation map of an input within a single architecture. Both tasks share weights along the encoding part of the network (Sec. 2.1) and then separate into two distinct parts to model their different dimensionality. For the regression of the landmark positions we follow the architecture of the localization task (L), while for the semantic segmentation we employ residual learning with up-sampling layers as in [10]. Here, our goal is to predict for each pixel its probability belonging to a specified class, e.g. manipulator, shaft or background. With consideration to real-time constraints, we only allow the network to produce an output at half the input resolution and bi-linearly up-sample the result. By sharing the encoder weights, the two tasks can influence each other while upholding their own objectives. The training sample in this case is (X, S, y) , and the prediction consists of $\tilde{S} \in \mathbb{R}^{\frac{w}{2} \times \frac{h}{2} \times c}$ and $\tilde{y} \in \mathbb{R}^{2 \times n}$. The network is trained by combining the losses for the separate tasks: $l_{SL}(\tilde{y}, y, \tilde{S}, S) = \lambda_L l_L(\tilde{y}, y) + l_S(\tilde{S}, S)$. Here, λ_L balances the influence of both loss terms. For the segmentation loss we employ a pixel-wise softmax-log loss.

$$l_S(\tilde{S}, S) = -\frac{1}{wh} \sum_{x=1}^w \sum_{y=1}^h \sum_{j=1}^c S(x, y, j) \log \left(\frac{e^{\tilde{S}(x,y,j)}}{\sum_{k=1}^c e^{\tilde{S}(x,y,k)}} \right) \quad (1)$$

Concurrent Segmentation and Localization (CSL): In both L and SL architectures, only a single 2D position is considered as the correct target for each landmark. In this model (Fig. 2, CSL), we address this discrepancy, which can also arise due to imprecise labeling, by regressing a heatmap for each tracked landmark instead of its exact coordinates. The heatmap represents the confidence of being close to the correct location of the tracked point, and is created by applying a Gaussian kernel to the point’s location. The heatmaps have the same size as the segmentation and can explicitly share the weights of the entire network. We further augment the architecture with long-range skip connections that *sum* lower-level feature maps from the encoding into the decoding stage, in addition to the residual connections on the up-sampling layers [10]. This allows higher resolution information from the initial layers to be directly available at the output layers without being compressed in the encoding part of the architecture, thus increasing the accuracy. Finally we enforce the strong dependency of the two tasks by separating them only at the very end and concatenating the predicted segmentation features (before softmax) to the last feature-map of the network as an auxiliary means before regressing the location heatmaps. The overall loss is given by:

$$l_{CSL} = l_S(\tilde{S}, S) + \frac{\lambda_H}{n} \sum_{i=1}^n \sum_{x=1}^w \sum_{y=1}^h \left\| \frac{1}{\sqrt{2\pi\sigma^2}} e^{-\frac{\|y_i - (x,y)^T\|_2^2}{2\sigma^2}} - \tilde{y}_{x,y,i}^* \right\|_2^2 \quad (2)$$

The standard deviation σ controls the spread of the Gaussian around the landmark location y_i . In testing, the point of maximum confidence in each predicted heatmap $\tilde{y}_i^* \in \mathbb{R}^{\frac{w}{2} \times \frac{h}{2} \times n}$ is used as the location of the instrument landmarks.

3 Experiments and Results

In this section, we evaluate the performance of the proposed method in terms of localization of the instrument landmarks, as well as segmentation accuracy.

Datasets: We evaluate on two different datasets. The **Retinal Microsurgery Dataset** [3] consists of 18 sequences of *in-vivo* retinal microsurgery, each with 200 frames of resolution 1920×1080 pixels. The set is further classified into four different, instrument-dependent subsets. The annotated tool joints are $n = 3$ and semantic classes $c = 2$ (tool, background). The **EndoVis Dataset** is a *robotic* dataset published for the Instrument Segmentation and Tracking Sub-challenge as part of the MICCAI 2015 Endoscopic Vision Challenge. The training data contains four *ex-vivo* sequences of 45s and the testing four 15s and two 60s videos. All sequences have a resolution of 720×576 pixels and 25 fps. There is $n = 1$ joint and the $c = 3$ semantic classes are manipulator, shaft, background.

Implementation details: The encoder is initialized with ResNet-50 weights pretrained on ImageNet. All newly added layers are initialized as random filters sampled from a normal distribution with zero mean and 0.01 variance. During training, we apply photometric and geometric augmentations. All images are first resized to 640×480 pixels and then augmented with small random rotations

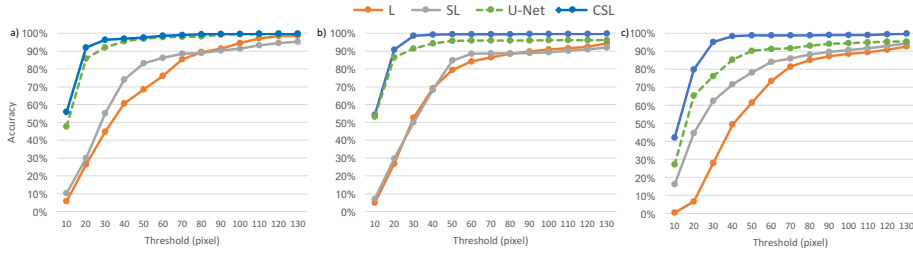


Fig. 3. Evaluation of Modeling Strategies: Accuracy of the models by means of Threshold Score for the left tip (a), right tip (b) and center joint (c) of the instrument.

$[-5^\circ, 5^\circ]$, resizing with scale $[1, 1.2]$, random crops of 480×480 , gamma correction with $\gamma \in [0.9, 1.1]$ and a multiplicative color factor in $[0.8, 1.2]$ for each channel. For the localization, we set $\sigma = 5$ for RM and $\sigma = 7$ for **EndoVis** in which the tools are larger. All CNNs are trained with stochastic gradient descent with a learning rate of 10^{-7} , momentum of 0.9 and $\lambda_L, \lambda_H = 1$. The inference time is 56ms per frame on a NVIDIA GeForce GTX TITAN X using MatConvNet. We employ the general Threshold Score and the *KBB* Score [3], which addresses the quality of the keypoint predictions as a pixel-wise measure normalized by the size of the manipulator. The segmentation is evaluated by means of DICE score.

3.1 Evaluation of Modeling Strategies

First, we evaluate the models for instrument landmark localization by training on 9 sequences of the RM dataset and testing on the remaining ones. In Fig. 3, the baseline of explicit 2D landmark localization (**L**) shows the lowest results, while its combination with a segmentation task (**SL**) increases the performance. The highest accuracy of over 90% for both tool tips and 79% for the center joint (thres. 20 pixels), is achieved by the proposed **CSL**. Our model exploits contextual information for precise localization of the tool, by sharing feature maps with the semantic segmentation task. Another baseline is the U-Net architecture [14] trained with our losses. CSL is consistently more accurate in localization and achieves a DICE score of 75.4%, while U-Net scores 72.5% for segmentation. SL achieves a DICE score of 73.7% and CSL without skip connections 74.4%.

3.2 Retinal Microsurgery

Analogously to [3], we train on all first halves of the 18 RM sequences and evaluating on the remaining frames, referred to as *Half Split*. As shown in Fig. 4, the proposed method clearly outperforms the state-the-art-methods, reaching an average accuracy of more than 84% considering the *KBB* score with $\alpha = 0.15$. Next, we evaluate the generalization ability of our method not only to unseen sequences and but also unknown geometry. We employ a leave-one-out scheme on the subsets given by the 4 different instrument types, referred to as *Cross Validation*. Also here, our method achieves state-of-the-art performance.

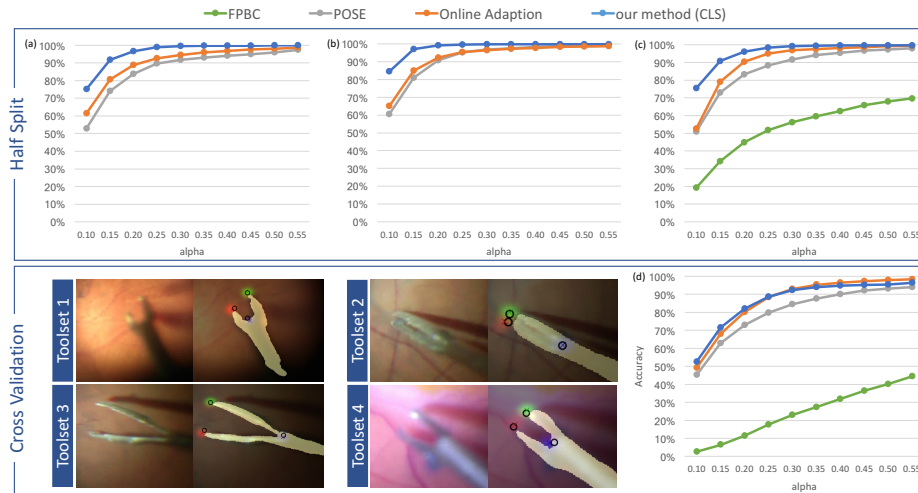


Fig. 4. RM dataset: Comparison to FPBC [15], POSE [3] and Online Adaption [6], measured by the metric *KBB*. The charts (a) to (c) show the accuracy for the left tip, right tip and center joint, respectively, for the *Half Split* experiment. In the *Cross Validation*, the training set is given by 3 instrument dependent subsets and the method is tested on the remaining set. (d) shows the average *KBB* score for the center point.

3.3 EndoVis Challenge

For this dataset, we performed our experiments in a leave-one-surgery-out fashion, as specified by the guidelines. The quantitative results are depicted in table 1. The challenging aspect of this dataset is that either one or two instruments (left and right) can be present in the video. To alleviate this problem, we additionally appended random horizontal flips as data augmentation, such that the instrument is at least seen from both sides. In Sets 5 and 6, the network was capable of successfully localizing and segmenting a previously unseen instrument and viewpoint⁵. Evaluating on set 1 is impossible as the training sets contain one tool only, while the test set always contains both.

Dataset	Set 2	Set 3	Set 4	Set 5	Set 6
Avg. loc. error (pixel)	9.7	10.9	13.0	38.4/60.0	36.4/63.9
Seg. Precision (%)	96.5	93.5	83.1	83.0	80.8
Seg. Recall (%)	89.8	90.1	89.6	88.5	86.6
Seg. DICE (%)	93.0	91.6	85.8	85.5	83.5

The average localization for set 5 and 6 is for the left and right instrument, respectively. Seg. results refer to the binary labelling.

Table 1. Quantitative Results for EndoVis.



Fig. 5. Qualitative Results.

⁵ the challenge administrators believe that the ground truth regarding tracking for sequence 5 and 6 is not as accurate as for the rest of the sequences.

4 Conclusion

In this paper, we propose to model the localization of instrument landmarks as a heatmap regression. This allows us to leverage deep-learned features via a CNN to concurrently regress the instrument segmentation and its articulated 2D pose in an end-to-end manner. We evaluate the performance on two different benchmarks and, throughout the experiments our approach outperforms state-of-the-art methods.

References

1. Bouget, D., Allan, M., Stoyanov, D., Jannin, P.: Vision-based and marker-less surgical tool detection and tracking: a review of the literature. *Medical Image Analysis* **35** (2017)
2. Sznitman, R., Richa, R., Taylor, R.H., Jedynek, B., Hager, G.D.: Unified detection and tracking of instruments during retinal microsurgery. *IEEE trans. on Pattern Analysis and Machine Intelligence* **35**(5) (2013)
3. Rieke, N., Tan, D.J., Amat di San Filippo, C., Tombari, F., Alsheakhali, M., Belagiannis, V., Eslami, A., Navab, N.: Real-time localization of articulated surgical instruments in retinal microsurgery. *Medical Image Analysis* **34** (2016)
4. Bouget, D., Benenson, R., Omran, M., Riffaud, L., Schiele, B., Jannin, P.: Detecting surgical tools by modelling local appearance and global shape. *Trans. on Medical Imaging* **34**(12) (2015)
5. Zhou, J., Payandeh, S.: Visual tracking of laparoscopic instruments. *J. Autom. Cont. Eng.* Vol. **2**(3) (2014)
6. Rieke, N., Tan, D.J., Tombari, F., Vizcaíno, J.P., di San Filippo, C.A., Eslami, A., Navab, N.: Real-time online adaption for robust instrument tracking and pose estimation. In: *MICCAI*. (2016)
7. Sarikaya, D., Corso, J.J., Guru, K.A.: Detection and localization of robotic tools in robot-assisted surgery videos using deep neural networks for region proposal and detection. *IEEE Transactions on Medical Imaging* (2017 (to appear))
8. Allan, M., Ourselin, S., Thompson, S., Hawkes, D.J., Kelly, J., Stoyanov, D.: Toward detection and localization of instruments in minimally invasive surgery. In: *IEEE Transactions on Biomedical Engineering* **60**, pp. 1050 – 1058 (2013)
9. Reiter, A., Allen, P.K., Zhao, T.: Marker-less articulated surgical tool detection. In: *Computer assisted radiology and surgery*. (2012)
10. Laina, I., Rupprecht, C., Belagiannis, V., Tombari, F., Navab, N.: Deeper depth prediction with fully convolutional residual networks. In: *Int. Conf. on 3D Vision (3DV)*, IEEE (2016)
11. He, K., Zhang, X., Ren, S., Sun, J.: Deep residual learning for image recognition. In: *Int. Conf. on Computer Vision and Pattern Recognition*. (2016)
12. Alsheakhali, M., Eslami, A., Navab, N.: Detection of articulated instruments in retinal microsurgery. In: *Biomedical Imaging (ISBI)*, 2016, IEEE (2016)
13. Rupprecht, C., Lea, C., Tombari, F., Navab, N., Hager, G.D.: Sensor substitution for video-based action recognition. In: *Intelligent Robots and Systems, IEEE* (2016)
14. Ronneberger, O., Fischer, P., Brox, T.: U-net: Convolutional networks for biomedical image segmentation. In: *MICCAI*, Springer (2015)
15. Sznitman, R., Becker, C., Fua, P.: Fast part-based classification for instrument detection in minimally invasive surgery. In: *MICCAI 2014*, Springer (2014)